Available online at www.sciencedirect.com
SCIENCE DIRECT®
International Journal of Thermal Sciences 42 (2003) 1047–1059
International Journal of Thermal Sciences
www.elsevier.com/locate/ijts

Fluid flow and mixed convection heat transfer in a rotating curved pipe

Huajun Chen *, Benzhao Zhang

Department of Mechanics, Zhejiang University, Hangzhou, 310027, People's Republic of China

Received 19 July 2002; accepted 7 March 2003

Abstract

When a temperature-induced variation of fluid density occurs in a rotating curved pipe, the Coriolis force, the centrifugal-type buoyancy force and the centrifugal force will contribute to the generation of the secondary flow. The interaction of these body forces complicates the characteristics of flow and heat transfer. A numerical study is performed to examine the combined effects of rotation (Coriolis force), curvature (centrifugal force) and heating/cooling (centrifugal-type buoyancy force), and solutions are obtained for a wide range of parameters. The combined effects of these comparable order of magnitude forces on the flow structure, temperature distribution, friction factor and Nusselt number are examined in detail. Present works show the natures of the flow and heat transfer in rotating curved pipes.

Keywords: Curved pipe; Mixed convection; Secondary flow; Rotation

1. Introduction

Since the initial work by Dean [1,2], the flow through a curved pipe has attracted more and more attentions not only because of its practical importance in various industrial applications, but also of physically interesting phenomena under the action of centrifugal force caused by curvature of the pipe. One of the main features is the generation of the secondary flow. Previous work on curved pipes is referred to in the review articles by Berger et al. [3], Nandakumar and Masliyah [4], Ito [5] and Berger [6].

When a pipe rotates about an axis normal to a plane including the pipe, the Coriolis force could also contribute to the generation of the secondary flow and the heat transfer becomes more complicated. Such rotating pipes have extensive applications, such as the cooling systems for conductors of electric generator motors, gas turbines, separation processes. The nature of the flow and heat transfer in rotating pipes is affected by the interaction of the imposed pressure-driven axial flow, the system rotation and the geometrical structure of the pipe. This interaction causes the fluid flow and heat transfer performance in a rotating pipe to be drastically different from those in a stationary case. Admittedly, the theoretical solutions and the experimental relations for the stationary cases are not valuable for the rotating ones.

On the other hand, when the fluid is heated or cooled, the centrifugal-type buoyancy force could also contribute to the secondary flow because of the temperature-induced variation of fluid density. These forces will result in three interactive kinds of secondary flow: the Coriolis-force driven, the buoyancy-force driven and the centrifugal-force driven secondary flow. Therefore complicated behaviors of secondary flow and axial flow are expected.

As an interesting topic, the combined effects of curvature and rotation had been examined by numerous researchers. Ludwieg [7] firstly analyzed the flow in a rotating toriodal rectangular pipe theoretically and developed a solution based on the integral method. Hocking [8] studied the flow in a high speed rotating pipe with the same method. Ito and Motai [9] first studied the fluid flow in both co-rotating and counter-rotating (the rotating angular velocity and the axial velocity are in the opposite directions) curved ducts and predicted a reduction strength and a reversal of the direction of the secondary flow theoretically for a small parameter. Ito et al. [10,11] studied friction factors in a rotating toroidally curved pipe numerically and experimentally for the cases of constant Dean number. But their computations were limited to relatively small parameters. Daskopoulos and Lenhoff [12], Selmi et al. [13] concerned their works on the bifurcation of the flow in rotating curved pipes with circular and square cross section. Ishigaki [14–16] examined

* Corresponding author.
E-mail address: mec_zbzq@emb.zju.edu.cn (H. Chen).

1290-0729/$ – see front matter
doi:10.1016/S1290-0729(03)00088-7

Nomenclature

d_H	hydrodynamic diameter, $=2R_c$	m	
Dn	Dean number, $=Re\kappa^{1/2}$		
f_c, Nu_c	friction factor and Nusselt number		
f_s, Nu_s	friction factor and Nusselt number for a stationary straight pipe		
F	rotational number, $=\Omega^* R/w_m^*$		
p^*	pressures	Pa	
P	dimensionless general pressure, $P=p-\frac{1}{2}\Omega^2(1+\kappa r\cos\theta)^2-\Omega^2 r\cos\theta$		
Pr	Prandtl number, $=\frac{\nu}{\alpha}$		
q_w	wall heat flux	$\mathrm{W\cdot m^{-2}\cdot K^{-1}}$	
R	curvature radius of the centerline of the pipe	m	
R_c	radius of the pipe	m	
Ra_Ω	rotational Rayleigh number, $=\beta R\Omega^{*2}d^3\Delta T^*/\nu^2$		
Re	Reynolds number, $=W_m^* d_H/\nu$		
r^*	radial direction coordinates	m	
s^*	axial direction coordinates	m	
T^*, T_w^*	temperature of fluid and wall	(°C, K)	
u^*, v^*, w^*	physical velocity components	$\mathrm{m\cdot s^{-1}}$	
w_m^*	dimensional mean axial velocity	$\mathrm{m\cdot s^{-1}}$	
X, Y	coordinates of the cross section		

Greek symbols

α	thermal diffusivity	$\mathrm{m_2\cdot s^{-1}}$
β	coefficient of thermal expansion	$\mathrm{K^{-1}}$
ν	kinematic viscosity of fluid	$\mathrm{m\cdot s^{-2}}$
κ	dimensionless curvature	
Ω	dimensionless rotating angular velocities	
θ	angular coordinate	
ρ	density of the bulk fluid	$\mathrm{kg\cdot m^{-3}}$
ρ_w	density of the fluid near the wall	$\mathrm{kg\cdot m^{-3}}$
ψ	dimensionless stream function	
ΔT^*	representative temperature difference $=Pr\,d_H\partial T^*/\partial s^*$	(°C, K)
Θ	dimensionless temperature	

flow structure and heat transfer numerically for both counter-rotating and co-rotating curved pipes with a small curvature and a circular cross-section and he obtained the semi-empirical formulae for average frication factor and heat transfer rate. Zhang et al. [17] theoretically studied the same problem of Ishigaki [15] using the perturbation method.

However, the works mentioned above focused merely on the combined effects of the Coriolis force and the centrifugal force on the flow, and the effects of centrifugal-type buoyancy force received relatively scant attention. Miyazaki [18,19] firstly took all the three body forces into account, and studied the characteristics of the flow and heat transfer in curved circular and rectangular pipes with spanwise rotation and heating effects and pointed out that the wall shear stress increased with increasing rotating speed. But he did not show the solution when the three body forces are of comparable order of magnitude. Moreover, there also exist some errors in the viscous terms of the governing equations. Wang and Cheng [20], employing finite volume method, examined the flow characteristics and heat transfer in curved square pipes when the three body forces are of comparable order of magnitude. The flow transitions of the secondary flow and the main flow and their effects on temperature distribution were shown in detail, and the primary instabilities (centrifugal, Coriolis and buoyancy force instabilities) were also involved in their works. But their studies were only limited in the positive case of the square cross-section duct and they did not take the counter-rotating case into account.

Based on the works mentioned above, we can find that there isn't any study on the flow and the mixed heat transfer in circular pipes with simultaneous effects of curvature, rotation and heating/cooling, and the counter-rotating pipe flow receives little attention. To bridge the gap, we present a comparatively comprehensive numerical study on the fluid flow and the mixed convection heat transfer in a rotating circular pipe in this paper. The effects of the comparable order of magnitude forces (the centrifugal force, the Coriolis force and the centrifugal-type buoyancy force) on the flow behaviors, temperature distributions, the friction factor and the Nusselt number are examined in detail.

2. The governing equations

Fig. 1 shows the curved pipe rotating around the axis $O'A$ with a constant angular velocity Ω^*. As in Fig. 1, the coordinate (r^*, θ, s^*) is fixed on the rotating pipe, and the origin o is on the centerline of the pipe. The radius of the pipe is R_c and the velocity components in the directions of r^*, θ, s^* are denoted by u^*, v^*, w^*, respectively. When $\Omega^* > 0$, the rotation has the same direction with the axial velocity (co-rotation) and when $\Omega^* < 0$, the rotation and the axial velocity are in the opposite directions (counter-rotation).

It is assumed that the fluid flow is steady, laminar, hydrodynamically and thermally fully developed, the wall heat flux q_w and the peripheral wall temperature T_w are both uniform. Heat conduction in the direction of pipe axis is neglected. If the fluid density is constant, the rotational centrifugal force does not make any contribution to the motion of the fluid, since the force is balanced by a pressure gradient in the X direction. However, when the temperature-induced variation of fluid density is taken into account, the rotational centrifugal force becomes locally nonuniform and gives rise to a fluid motion in the form of a buoyancy force.

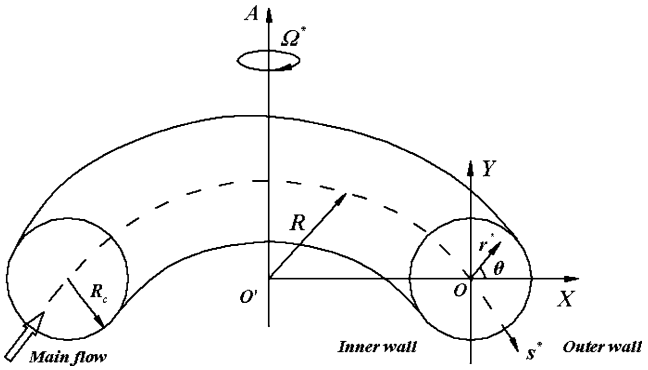

Fig. 1. The rotating pipe and the coordinate system.

By the Bossinesq approximation, the density variation with temperature is according to the relation

$$\begin{aligned}\rho &= \rho_w + \rho_w\beta\left(T_w^* - T^*\right)\\ &\approx \rho_w + \rho\beta\left(T_w^* - T^*\right) \quad \text{since } \rho_w \approx \rho\end{aligned} \tag{1}$$

where β is the coefficient of thermal expansion. Therefore, using Eq. (1), the rotational centrifugal force per unit volume is expressed as

$$\begin{aligned}&\rho\Omega^{*2}(R + r^*\cos\theta)\\ &\quad= \rho_w\Omega^{*2}(R + r^*\cos\theta)\\ &\qquad+ \rho_w\Omega^{*2}\beta(R + r^*\cos\theta)\left(T_w^* - T^*\right)\\ &\quad\approx \rho_w\Omega^{*2}(R + r^*\cos\theta)\\ &\qquad+ \rho\Omega^{*2}\beta(R + r^*\cos\theta)\left(T_w^* - T^*\right)\end{aligned} \tag{2}$$

Then we introduce the general pressure as

$$P^* = p^* - \frac{1}{2}\rho\Omega^{*2}(R + r^*\cos\theta)^2 \tag{3}$$

The dimensionless variables are defined as

$$s = \frac{s^*}{d_H}, \qquad r = \frac{r^*}{d_H}, \qquad w = \frac{w^*}{W_m^*}, \qquad u = \frac{u^* d_H}{\nu}$$

$$v = \frac{v^* d_H}{\nu}, \qquad P = \frac{P^* d_H^2}{\rho\nu^2}, \qquad \Theta = \frac{T_w^* - T^*}{\Delta T^*}$$

$$\Omega = \frac{\Omega^* d_H^2}{\nu}$$

Where ν is the kinematic viscosity and ρ is the fluid density; d_H is the hydrodynamic diameter defined as $d_H = 2R_c$; W_m^* is dimensional mean axial velocity; p is the dimensional pressure; Θ is the dimensional temperature; ΔT^* is the temperature difference, which is defined as $Pr\, d_H \partial T^*/\partial s^*$, here Pr is the Prandtl number.

Accordingly, the continuity, momentum and energy equations governing the fully developed laminar flow and heat transfer can be obtained in terms of dimensionless variables as

$$\frac{\partial(rMu)}{\partial r} + \frac{\partial(Mv)}{\partial\theta} = 0 \tag{4}$$

$$\begin{aligned}&u\frac{\partial u}{\partial r} + \frac{v}{r}\frac{\partial u}{\partial\theta} - \frac{v^2}{r} - Dn^2\frac{\cos\theta}{M}w^2\\ &\quad= -\frac{\partial P}{\partial r} + 2F\,Dn^2 w\cos\theta + Ra_\Omega\Theta M\cos\theta\\ &\qquad+\left[\nabla^2 u - \frac{2}{r^2}\frac{\partial v}{\partial\theta} - \frac{1}{r^2}u + \frac{\kappa v\sin\theta}{rM}\right.\\ &\qquad\left.+\frac{\kappa^2\cos\theta}{M^2}(v\sin\theta - u\cos\theta)\right]\end{aligned} \tag{5}$$

$$\begin{aligned}&u\frac{\partial v}{\partial r} + \frac{v}{r}\frac{\partial v}{\partial\theta} + \frac{uv}{r} + Dn^2\frac{\sin\theta}{M}w^2\\ &\quad= -\frac{1}{r}\frac{\partial P}{\partial\theta} - 2F\,Dn^2 w\sin\theta + Ra_\Omega\Theta M\sin\theta\\ &\qquad+\left[\nabla^2 v + \frac{2}{r^2}\frac{\partial u}{\partial\theta} - \frac{1}{r^2}v - \frac{\kappa u\sin\theta}{rM}\right.\\ &\qquad\left.-\frac{\kappa^2\sin\theta}{M^2}(v\sin\theta - u\cos\theta)\right]\end{aligned} \tag{6}$$

$$\begin{aligned}&u\frac{\partial w}{\partial r} + \frac{v}{r}\frac{\partial w}{\partial\theta} + \frac{\kappa\cos\theta}{M}uw - \frac{\kappa\sin\theta}{M}vw\\ &\quad= -\frac{\sqrt{\kappa}}{Dn}\frac{\partial P}{\partial s} - 2F\kappa(u\cos\theta - v\sin\theta)\\ &\qquad+\left(\nabla^2 w - \frac{\kappa^2\cos\theta}{M^2}w\right)\end{aligned} \tag{7}$$

$$Pr\left(u\frac{\partial\Theta}{\partial r} + \frac{v}{r}\frac{\partial\Theta}{\partial\theta}\right) - \frac{Dn}{M\sqrt{\kappa}}w = \nabla^2\Theta \tag{8}$$

where

$$\nabla^2 = \frac{1}{rM}\left[\frac{\partial}{\partial r}\left(rM\frac{\partial}{\partial r}\right) + \frac{1}{r}\frac{\partial}{\partial\theta}\left(M\frac{\partial}{\partial\theta}\right)\right]$$

$$M = 1 + \kappa r\cos\theta$$

From above equations, it can be easily drawn that the flow in a rotating curved pipe with circular cross-section is affected by the following parameters:

The curvature κ: $\kappa = d_H/R$, representing the ratio of the centrifugal force to the inertial force.

The Dean number Dn: $Dn = Re\sqrt{\kappa}$ ($Re = w_m^* d_H/\nu$), a square root of the product of (inertial force/viscous force) and (centrifugal force/viscous force).

F number: $F = \Omega^* R/w_m^*$, representing the ratio of the Coriolis force to centrifugal force. $F > 0$ means co-rotation case, $F < 0$ means counter-rotation case, $F = 0$ means the stationary case.

The rotational Rayleigh number Ra_Ω: $Ra_\Omega = \beta R\Omega^{*2} d^3\Delta T^*/\nu^2$, representing the ratio of the centrifugal-type buoyancy force to the viscous force, a positive Ra_Ω represents the heating case while a negative Ra_Ω is for a cooling case.

The Prandtl number Pr: $Pr = \nu/\alpha$, it is a thermophysical property parameter, representing the ratio of momentum diffusion rate to that of thermal diffusion.

The stream function $\psi = \psi(r,\theta)$ is defined according to

$$\frac{1}{r}\frac{\partial\psi}{\partial\theta} = Mu, \qquad -\frac{\partial\psi}{\partial r} = Mv \tag{9}$$

So the continuity equation meets itself.

In this work, we attempt to examine the symmetric flow structure and temperature distribution with respect to the

horizontal centerline (X-axis) only. The solution domain is reduced to half of the pipe cross section. The problem boundary conditions can be given as

$$u = v = w = \Theta = 0 \tag{10}$$

in the pipe wall and

$$\frac{\partial u}{\partial \theta} = \frac{\partial w}{\partial \theta} = \frac{\partial \Theta}{\partial \theta} = 0 \tag{11}$$

in the symmetry plane (X-axis)

The imposition of the symmetry condition about the horizontal line constrains us to consider the symmetric solutions only. However, when the control parameter exceeds a critical value, the asymmetric solutions will occur due to (appearance of) the instabilities of this physical problem. Such analyses on the multiple solutions are beyond the scope of the present study. Although the instability will cause the flow to be asymmetric in some high control parameters region. To carry out a symmetric analysis appears still worthwhile in the senses that (1) the flow from such analyses forms the base flow which one must know in order to make instability analyses, and (2) such an analysis would indicate where in the control parameter space one should make the higher order instability analyses (Wang and Cheng [20]).

3. Numerical method of solution

The governing equations (1)–(5) are a set of convection-diffusion equations with velocity–pressure coupling. In order to obtain solutions for this kind of equations, we chose the finite-volume method to solve this problem. The power-law scheme is adopted to discretize the convection term and the SIMPLE scheme is employed to deal with the problem of velocity–pressure coupling. The mesh system is staggered and an alternating direction line-by-line iterative method (ADI) with the block correction technique is used to solve the discretization equations. The description of the numerical implementation can be found, for example, in Patankar [21].

In order to examine the accuracy of the calculation code, we first make the initial calculation by setting $Ra_\Omega = 0$ (without the effect of Buoyancy force). The friction factor ratio f_c/f_s and the Nusselt number ratio Nu_c/Nu_s for a rotating curved pipe obtained by the present analysis, together with the available numerical and experimental results, are shown as a function of F in Fig. 2. Here, f_s and Nu_s are the non-rotating straight pipe values at the same conditions. The figure shows that present results are in a good agreement with other results when Dn is moderate. When Dn is large, the results of this paper agree with the experimental results better than that of Ishigaki [15,16]. The reason for this is that Ishigaki [15,16] simplified the equation without taking the effect of high order terms of curvature into account.

In order to check the grid dependence, five types of grid sizes in the flow domain have been examined. Table 1 gives

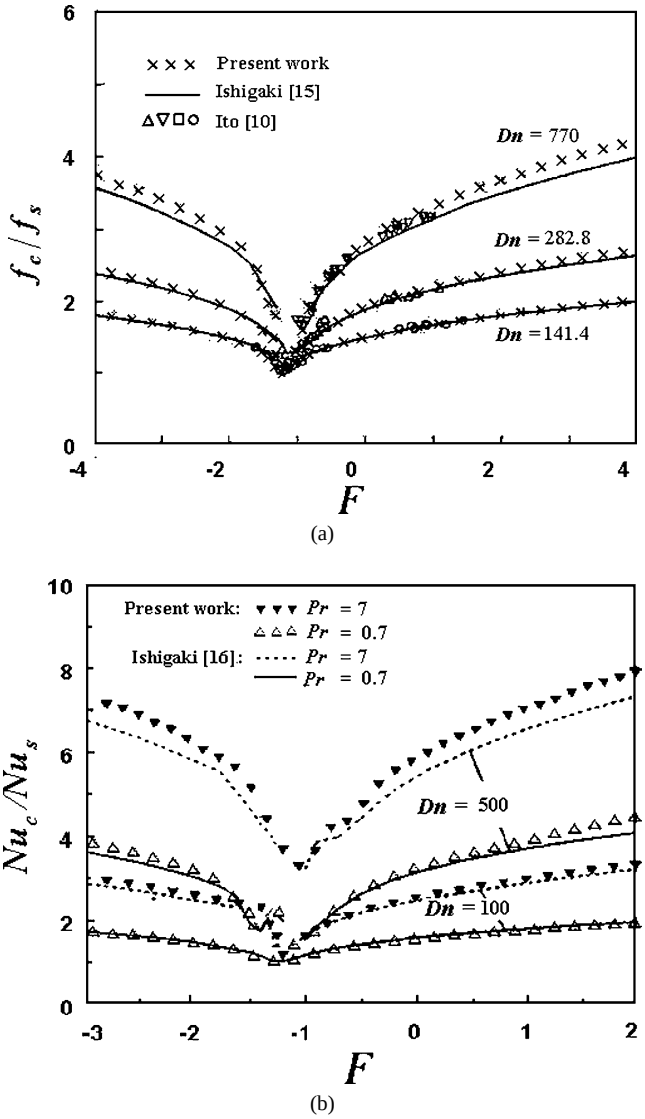

Fig. 2. Comparison with available experimental and computational results ($\kappa = 0.02$, $Ra_\Omega = 0$): (a) Variation of f_c/f_s with F; (b) Variation of Nu_c/Nu_s with F.

comparison on the maximum of axial velocity, friction factor ratios and the maximum of stream function of different grid systems with former numerical results. Calculations for $Dn = 100$, $\kappa = 0.1$, $F = -1.5$, and $Ra_\Omega = 0$ were carried out. We can see that there is less than 1% difference of the maximum axial velocity and friction factor ratios for the grid system 22×32, 32×42, 42×62 and 42×72. To save the CPU time, the grid system 32×42 is adopted for this problem.

4. Results and disscussion

A remarkable characteristic of the flow and the heat transfer in this problem is the simultaneous presence of centrifugal, Coriolis and centrifugal-type buoyancy forces, which induce three kinds of secondary flow in the plane of

Table 1
Grid test ($Dn = 100$, $\kappa = 0.1$, $F = -1.5$, $Ra_\Omega = 0$)

Grid system	w_{max}		f_c/f_s		ψ_{max}	
$M(r) \times N(\theta)$	Present work	Zhang [22]	Present work	Zhang [22]	Present work	Zhang [22]
12×32	1.7838		1.3239		4.7509	
22×32	1.8002		1.3395		4.8527	
32×42	1.8043	1.7983	1.3437	1.3409	4.8934	4.9072
42×62	1.8054		1.3485		4.9123	
42×72	1.8062		1.3492		4.9164	

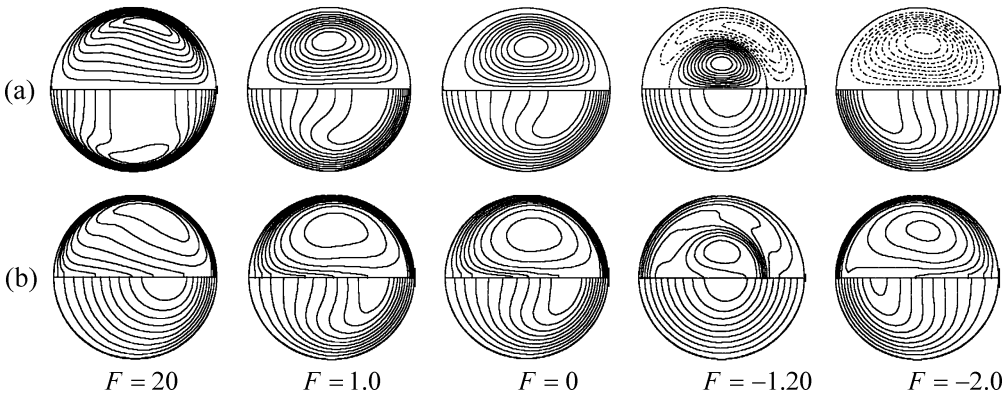

Fig. 3. (a) Contours of secondary flow (upper-half) and axial velocity (lower half), (b) Temperature distributions: $Pr = 40$ (upper-half), $Pr = 0.71$ (lower half) for $Dn = 100$, $\kappa = 0.2$, and $Ra_\Omega = 0$.

cross section. And as a result, this makes the flow structure and temperature more complicated.

Before discussion the characteristics of flow and heat transfer, we first analyze the effects of these body forces on flow. Due to the effect of curvature, the centrifugal force always points to the outer bend and pushes the high axial velocity to the outer bend. Meanwhile, the direction of the centrifugal-type buoyancy force (direction) depends on heating/cooling, when the fluid is heated, the buoyancy force points to the outer bend while the buoyancy force points to the inner bend when the fluid is cooled. While the centrifugal and buoyancy forces act on the plane of cross section, the Coriolis force has both X and s^* components. One component of Coriolis force in the X direction is $-2\Omega^* w^*$, which is caused by axial velocity and contributed to the generation of secondary flow, and another component in the s^* direction is $-2\Omega^* u_0^*$, which is caused by the secondary flow in the X direction and accelerates or decelerates the main flow. Either the Coriolis or buoyancy forces enhancing the centrifugal force is depending on the rotation or heating/cooling.

From the governing equations, we can see that the flow and the heat transfer under the consideration are characterized by five dimensionless parameters: Dn, κ, F, Ra_Ω, and Pr. Since F represents the ratio of the Coriolis force to the centrifugal force and Ra_Ω denotes the ratio of the centrifugal-type buoyancy force to the viscous force, we will keep Dn, κ and Pr as constants for each case, while changing F and Ra_Ω successively to check the combined effects of rotation and heating/cooling on the flow and heat transfer. However, it is still a lengthy process to describe the typical results covering the whole range of the parameters. So the results shown in this paper will be mainly confined as $\kappa = 0.2$, $Pr = 0.71$ or 40 and $Dn = 100$ or 500. In the figures, the stream function, axial velocity and temperature are normalized by their maximum absolute values ψ_{max}, w_{max}, and Θ_{max}, and the solid, dotted and dot-dash lines indicate positive, zero, negative values and the outer side of the pipe is on the right. A vortex with a positive (negative) value of stream function indicates a counter-clockwise (clockwise) circulation.

4.1. Flow behaviors and temperature distributions

4.1.1. The case without the effect of buoyancy force ($Ra_\Omega = 0$)

Fig. 3 illustrates the variation of flow behaviors and temperature distributions with F at $Dn = 100$, $\kappa = 0.2$, and $Ra_\Omega = 0$. For $F = 1.0$ (co-rotation), both the centrifugal force and the Coriolis forces act radially outwards and two kinds of secondary flow in the same direction are superimposed. As a result, the secondary flow still keeps the two-cell structure that has the same direction with the stationary case ($F = 0$) and the net secondary flow strength is merely intensified. The Coriolis force pushes the high axial velocity region more to the outer bend. We increase F further, when $F = 20$, the Taylor–Proudman effect appears, and here, two maximum axial velocity regions can be found in the cross-section and the axial iso-velocity lines are

almost constant in the rotational vector in the inviscid core of the flow. The detailed discussion for this phenomenon can be found in Miyazaki [19].

In the case of the counter-rotation, two kinds of secondary flow act in the opposite directions. When the strengths of two kinds of secondary flow are of the same magnitude, they can coexist in the cross-section, as seen in the case $F = -1.2$. Here, the effects of the two opposite secondary flows on the primary flow neutralize each other and the distributions of the axial flow are like the Poiseuille flow. As F decreases further, the increasing Coriolis force will dominate the flow, the centrifugal force-driven secondary vortex disappears and a completely reversal secondary flow structure can be obtained at $F = -2.0$, as a result, the maximum of axial velocity is pushed to the inner bend in this case.

Fig. 3(b) shows the variation of temperature distributions with rotation. Before we discuss the temperature distributions, we first analyze the effect of Prandtl number Pr on temperature distribution by the energy equation (8). From the equation, it is seen that the effect of Pr on heat convection only appears in the secondary flow term and axial convection by main flow is independent of Pr. When Pr is very small, the heat convection by secondary flow can be neglected and the energy equation can be expressed as

$$-\frac{Dn}{M\sqrt{\kappa}}w = \nabla^2\Theta \tag{12}$$

This equation is the heat conduction equation with a heat source and is similar to the convection equation in stationary straight pips with no body force. When Pr is almost equal to 1, the energy equation (8) will show similarity with Eq. (7) for a small F and the temperature distribution for this condition may be similar to the axial velocity distribution. When Pr is very large, the axial convection can be ignored and the energy equation (8) can be expressed as

$$Pr\left(u\frac{\partial\Theta}{\partial r} + \frac{v}{r}\frac{\partial\Theta}{\partial\theta}\right) = \nabla^2\Theta \tag{13}$$

From this equation, we can find that the secondary flow will decide the heat transfer characteristics. In this case, the isothermal lines outside the thermal boundary layer are strongly correlated with the streamline of secondary flow. Hence, we can find the Prandtl number determines the sensitivity of heat transfer to the secondary flow.

In Fig. 3(b), we show the temperature distribution for two cases of Pr. From the figures, it can be found the responses of the thermal field to the flow field are different depending on Pr. For $Pr = 0.7$ (see the lower half in the figures), the contours of temperature and axial velocity show a strong similarity for all values of F except $F = 20$. Since the secondary flow is weaker for a large F, the temperature distribution approaches to be parabolic as $F \to \infty$. Meanwhile, for $Pr = 40$ (see the upper half in the figures), the secondary flow governs the heat transfer characteristics and the isotherm shows the similarity for the secondary streamlines. In this case, the mixing effect due to the secondary flow in the core region is larger, here the maximum temperature difference becomes small and isothermal lines are thicker near the wall than in the core.

Next, we examine the case of $Dn = 500$. For the case of $F = 1$ (co-rotation), this situation is similar to flows of larger Dn in a stationary curved pipe. However, for the case of counter-rotation, there exists an evident difference between this case and that of $Dn = 100$ with variance of F. When $F \approx -1$, the instable phenomena appear due to strong but opposite secondary flows. When $F = -1.02$, it will be seen that the streamlines show three vortexes in upper-half domain: two of them are due to the centrifugal force and the Coriolis force, one is due to the flow instability (Dean instability, the vortex near the symmetrical line). The maximum axial velocity is divided into two locations. The potential sources of instability are centrifugal force and Coriolis force. The centrifugal force produces a secondary flow which moves towards the outer wall along the horizontal line and tends to raise flow instability, the secondary flow due to the Coriolis force pointing inwards acts as the disturbance at $\theta = 0$ near the outer wall, then the additional vortex is generated. As F decreases, the secondary flow due to Coriolis force and the additional vortex combine with each other because the same rotating direction ($F = -1.05$), the secondary flow due to centrifugal force becomes weak and completely disappears at $F = -1.20$. At this value, the axial velocity still has two maximum locations. At $F = -1.45$, because the increasing Coriolis force reduces the centrifugal force effect, the flow instability disappears and the vortex due to the centrifugal force reappears. As F decreases further, the increasing Coriolis force will dominate the flow.

Fig. 4(b) shows the variation of temperature distribution with F. The responses of the temperature distributions at various Pr to the flow field are basically the same as in the case of $Dn = 100$, thus supporting the similarity arguments.

4.1.2. The heating case ($Ra_\Omega > 0$)

If the fluid is heated, the centrifugal-buoyancy force can also contribute to the generation of the secondary flow and has the same direction as the centrifugal force. As a result, the buoyancy-force driven secondary flow and the centrifugal-force driven secondary flow are superimposed.

Fig. 5 shows the variation of flow patterns in the heating case at $Dn = 100$, $\kappa = 0.2$ for different F. As Ra_Ω increases, the buoyancy-force driven secondary flow is gradually intensified. For the case $F = 1$, the Coriolis force also acts radially outwards. So all the three kinds of secondary flow act in the same direction and the resultant secondary flow keeps the same structure with that in the case $Ra_\Omega = 0$. For $F = 20$, the large magnitude of the Coriolis force dominates the flow and the effect of heating on flow is without influence, so the flow patterns almost keep the same structure with the increase of Ra_Ω. However, for the counter-rotation, the Coriolis-force driven secondary flow

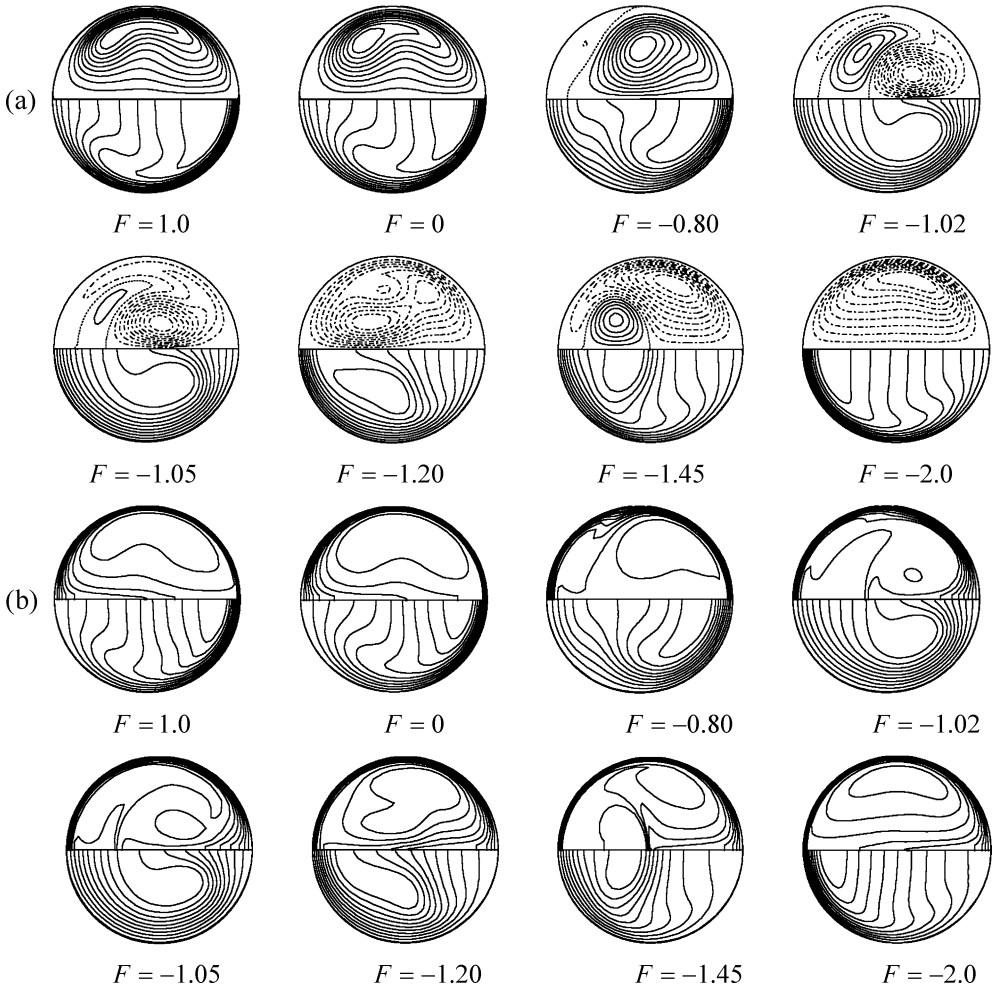

Fig. 4. (a) Contours of Secondary flow (upper-half) and axial velocity (lower half), (b) Temperature distributions: $Pr = 40$ (upper-half), $Pr = 0.71$ (lower half) for $Dn = 500$, $\kappa = 0.2$, and $Ra_\Omega = 0$.

acts in the opposite direction due to inward Coriolis force. So the buoyancy-force driven secondary flow neutralizes the Coriolis-force driven secondary flow gradually with the increasing of Ra_Ω. As seen in Fig. 5(c) ($F = -1.2$), when $Ra_\Omega = 0$, two kinds of secondary flow due to the Coriolis and centrifugal forces coexist in the cross-section and the location of the maximum axial velocity is near the center. As Ra_Ω increases, the secondary vortex due to the centrifugal force is intensified by the outward centrifugal-buoyancy force while the Coriolis-force driven secondary vortex is pushed to the inner wall and disappears gradually, and the location of axial velocity shifts toward the outer wall. For $F = -2$, when $Ra_\Omega = 1500$, the resultant secondary flow of buoyancy-driven and centrifugal forces almost has the same magnitude with that due to Coriolis force and then the coexistence of two kinds of secondary flow can also be found.

Fig. 6 illustrates the temperature distributions with Ra_Ω for two cases of Prandtl number, $Pr = 40, 0.71$. Just like the case without the effect of buoyancy force, the response of the thermal structure to flow structure depends on the Prandtl number. For the co-rotation cases, it will be seen that the increase of Ra_Ω almost has no evident variation on the thermal structure due to the three kinds of secondary flow acting in the same direction. However, for the counter-rotation, the effect of heating on the thermal structure is evident. For $Pr = 0.71$, the contours of temperature and axial velocity show a strong similarity and for $Pr = 40$, the contours of temperature are similar to those of secondary flow.

Now, we discuss the negative rotation case to study the interaction between inward Coriolis force and outward centrifugal and centrifugal-buoyancy forces for a large Dean number with increasing Ra_Ω. We take F as -2. For $Ra_\Omega = 0$, the secondary flow due to Coriolis force takes over the cross-section. In Fig. 7(a), when $Ra_\Omega = 7000$, the secondary vortex due to centrifugal-buoyancy force appears near the inner wall. As Ra_Ω increases, this vortex becomes stronger and moves toward the outer wall. When $Ra_\Omega = 12400$, the Coriolis-force driven secondary vortex is almost divided into two parts. As Ra_Ω increases further, the Coriolis-force driven secondary vortex shrinks gradually and shifts to the inner wall. Due to the large body forces, the contours of axial velocity appear as if they are pulled inward and outward

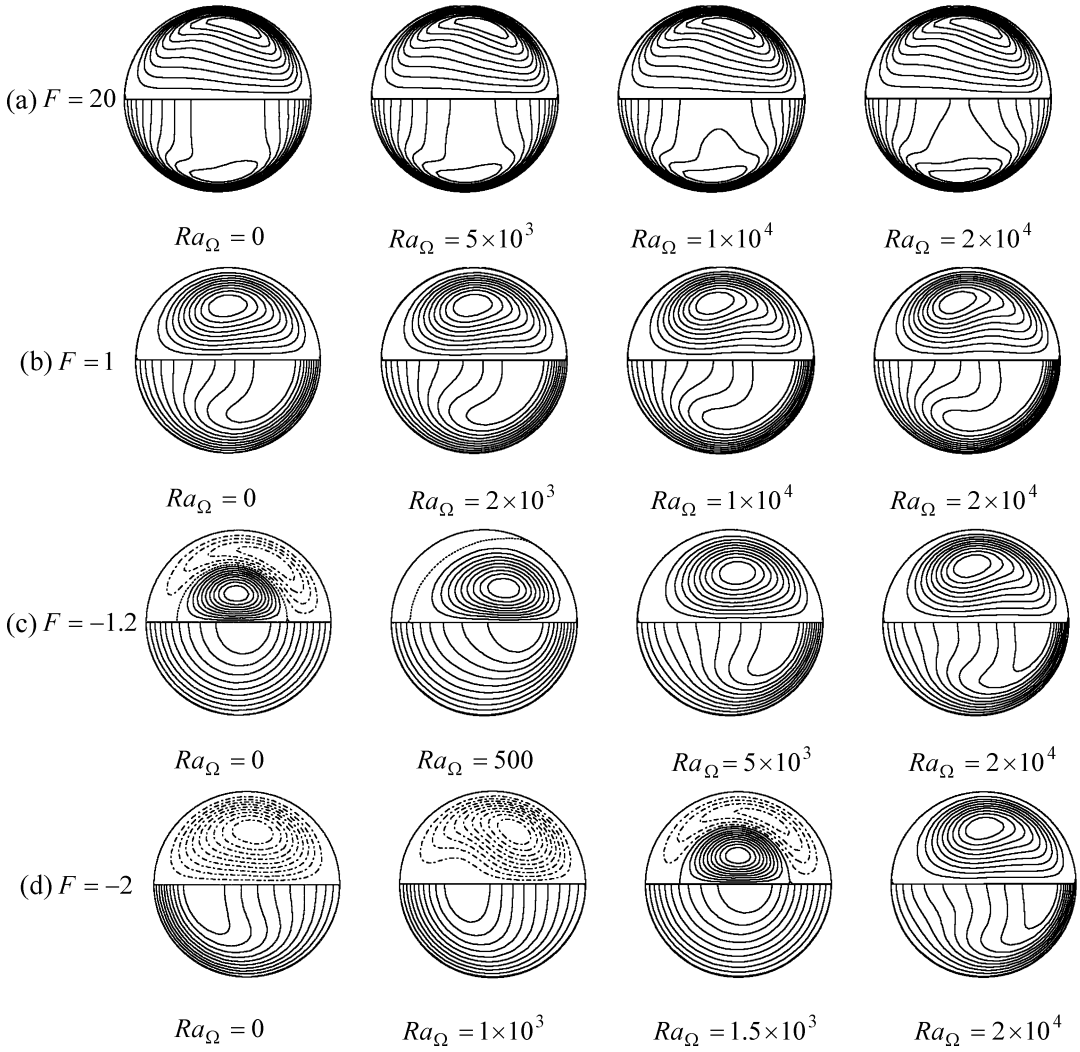

Fig. 5. Contours of secondary flow (upper-half) and axial velocity (lower half) for $Dn = 100$, $\kappa = 0.2$.

simultaneously in the range $Ra_\Omega = 12600$–30000. As seen in last section, when $F \approx -1$, the centrifugal instability will occur due to the disturbance of the Coriolis force at a large Dean number for the case without heating. But in this case, the phenomena of instability do not appear because the buoyancy-force driven secondary flow takes the same direction as that of the centrifugal force and the disturbance does not generate. Fig. 7(b) shows the variations of temperature distribution with Ra_Ω.

4.1.3. The cooling case ($Ra_\Omega < 0$)

If the fluid is cooled, the centrifugal-buoyancy force has the opposite direction with the centrifugal force. For the co-rotation case ($F > 0$), the buoyancy-force driven secondary flow acts in the opposite direction with the other two forces while for counter-rotation case ($F < 0$), it acts in the same direction with the Coriolis-force driven secondary flow.

Fig. 8 shows the variation of flow patterns in the cooling case at $Dn = 100$, $\kappa = 0.2$ for different F. In Fig. 8(b) ($F = 1$), when Ra_Ω decreases to the point, where $Ra_\Omega = -3.94 \times 10^3$, the buoyancy force almost has the same magnitude with the other two forces but in the opposite direction and the buoyancy-force driven secondary vortex emerges along the outer wall of the pipe, here, the maximum axial velocity region is pushed toward the center. As Ra_Ω decreases further, this vortex will dominate the flow. For the high rotating case ($F = 20$), as Ra_Ω decreases, the secondary flow almost keeps the same structure but two maximum axial velocity regions merge and the distribution of axial velocity likes that in the Poiseuille flow. For the counter-rotation, the buoyancy force will enhance the effect of Coriolis force. In Fig. 8(c) and (d), as Ra_Ω decreases, the Coriolis-force driven secondary vortex is intensified by the increasing of buoyancy force and finally takes up the whole cross-section. A similar case occurs, as the response of temperature distribution to flow structure is dependent on the Prandtl number. To make the paper compact, we do not show the variation of temperature distribution with Ra_Ω in this section.

Fig. 9 shows flow patterns for a larger value $Dn = 500$ at $F = -0.5$. In this case, the buoyancy force has the same

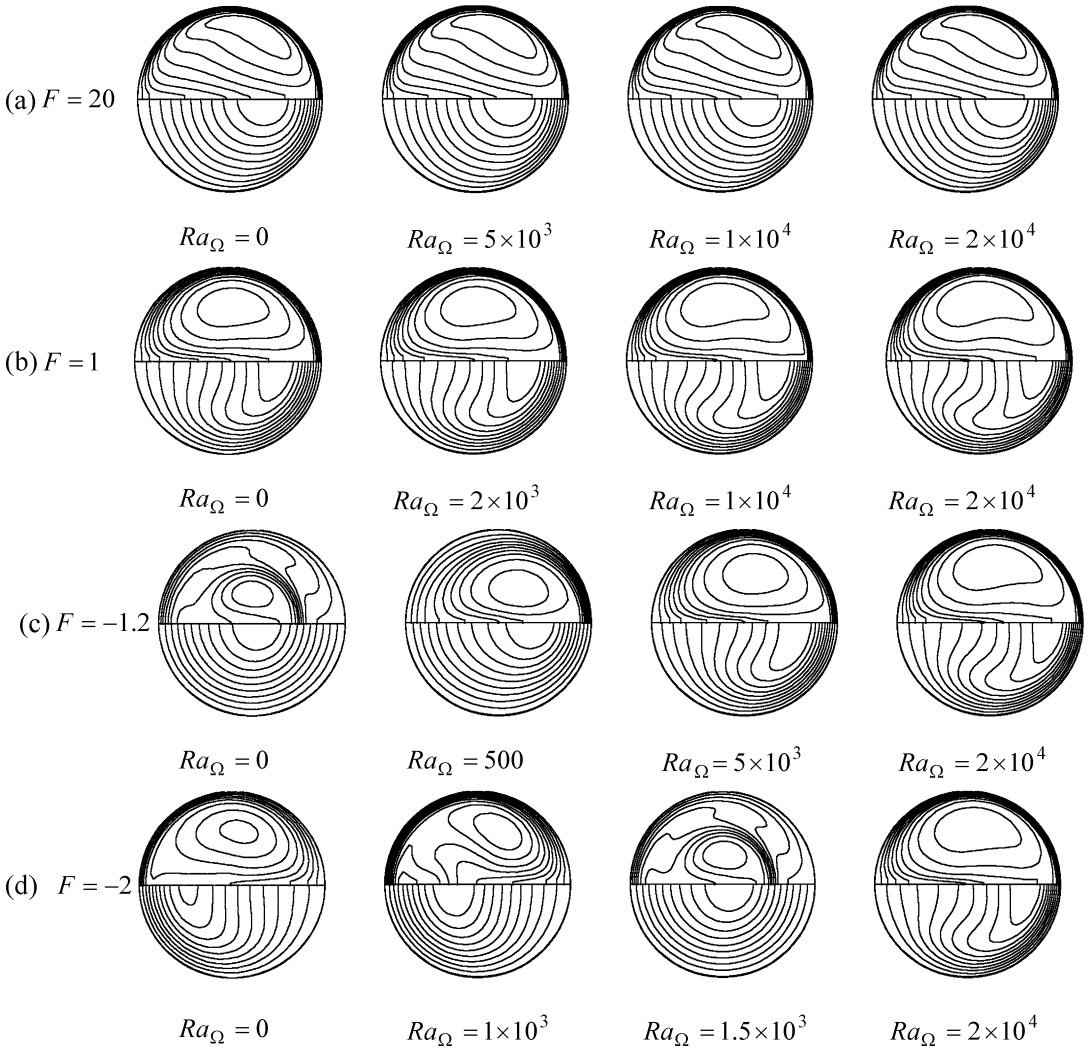

Fig. 6. Temperature distributions (upper-half: $Pr = 40$, lower half: $Pr = 0.71$) for $Dn = 100$, $\kappa = 0.2$.

direction with Coriolis force and points toward the inner wall. From the figures, we can find that the variation of flow patterns in this case is similar to that without the effect of buoyancy force. The buoyancy-force driven secondary flow could also act as the disturbance at $\theta = 0$ near the outer wall. When $Ra_\Omega = -6 \times 10^3$, the additional vortex due to the centrifugal instability occurs near the outer bend. As Ra_Ω decreases, the secondary flow due to buoyancy force and the additional vortex combine with each other. When $Ra_\Omega = -1 \times 10^4$, it will be seen that the instability phenomena disappear and the centrifugal force-driven vortex reappears. As Ra_Ω decreases, the inward buoyancy will dominate the flow.

4.2. Friction factor ratio and Nusselt number ratio

As two of the most important flow properties in engineering applications, the friction factor and the Nusselt number should be examined in details. First, we show the friction ration and Nusselt number ratio for moderate Dean numbers. Fig. 10 gives the variation of friction factor ratio f_c/f_s against Ra_Ω for different force ratios F. In the figure, all curves have their minimum about 1.0 at a critical value where three kinds of body forces counteract each other and the secondary flow reversal occurs, which indicates, at this point, the friction factor almost has the same value as in the non-rotating straight pipe. We mark this critical value as Ra'_Ω. For $Ra_\Omega > Ra'_\Omega$, f_c/f_s increases as Ra_Ω increases and for $Ra_\Omega < Ra'_\Omega$, f_c/f_s decrease as Ra_Ω increases. And also Ra'_Ω changes with F. For the co-rotation case ($F = 1$), cooling could make the friction factor decrease to the minimum. However, for the counter-rotation ($F = -2$), only heating could make the friction factor decrease to the minimum. The variation of Nusselt number ratio with Ra_Ω is shown in Fig. 11. Just like the variation of f_c/f_s with Ra_Ω, Nu_c/Nu_s also reaches its minimum around the Ra'_Ω for a given F where the heat transfer becomes the weakest. Fig. 12 shows the variation of the Nusselt number ratio with Ra_Ω for different Pr. The larger Pr is, the stronger the convective heat transfer by secondary flow becomes. So the Nusselt number ratio becomes larger for a larger Pr. As

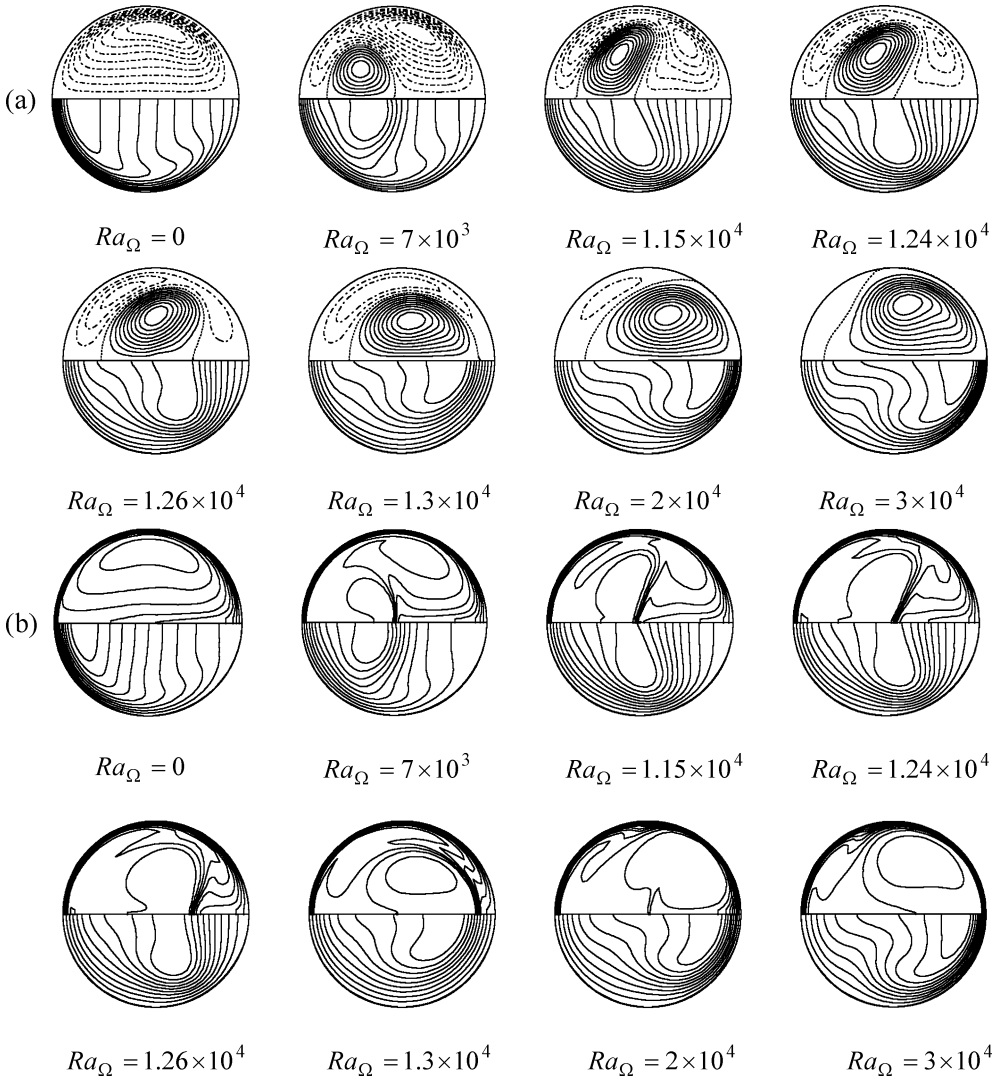

Fig. 7. (a) Contours of secondary flow (upper-half) and axial velocity (lower half), (b) Temperature distributions: $Pr = 40$ (upper-half), $Pr = 0.71$ (lower half) for $Dn = 500$, $\kappa = 0.2$, and $F = -2$.

seen in the figure, the increase of Pr enhances the heat transfer ratio evidently and the Nu_c/Nu_s-curve of a larger Pr is similar to that of a smaller Pr but with larger values.

The variation of friction factor ratio with Ra_Ω for a high rotating speed is shown in Fig. 12. Due to $F \gg 1$, the Coriolis force plays the main role on the flow and heating or cooling will intensify or weaken the effects of the Coriolis force. As shown in the figures, the f_c/f_s-curves increased almost in a parallel manner as F increases and for all the values of F, the friction factor ratio increases as Ra_Ω increases. Fig. 13 shows the variation of Nusselt number ratio with Ra_Ω at a high rotating speed. For different values of F, the Nusselt number ratio also increases as Ra_Ω increases. However, the Nu_c/Nu_s curves do not exhibit the parallel manner. Whether the increase of F increases the heat transfer ratio or not is dependent on the vale of Ra_Ω.

Fig. 15 shows the variations of friction factor ratio with Ra_Ω for different Dean numbers. Just like the case of a moderate Dean number, the f_c/f_s-curve for a larger Dean number also reaches its minimum value when Ra_Ω reaches a critical value. However, both of these this minimum values and the critical value are larger than those in the case for a smaller Dean number. The variations of Nusselt number ratio with Ra_Ω for different Dean numbers are illustrated in Fig. 16. For a larger Dean number, the Nu_c/Nu_s-curve almost shows the same manner with the f_c/f_s-curve in Fig. 15.

5. Conclusions

In this paper, the flow structure and mixed convection heat transfer in a rotating curved pipe have been investigated through computational studies. And we can see that the interaction of the Coriolis force, the centrifugal-type buoyancy force and the centrifugal force makes flow structure and heat transfer more complicated.

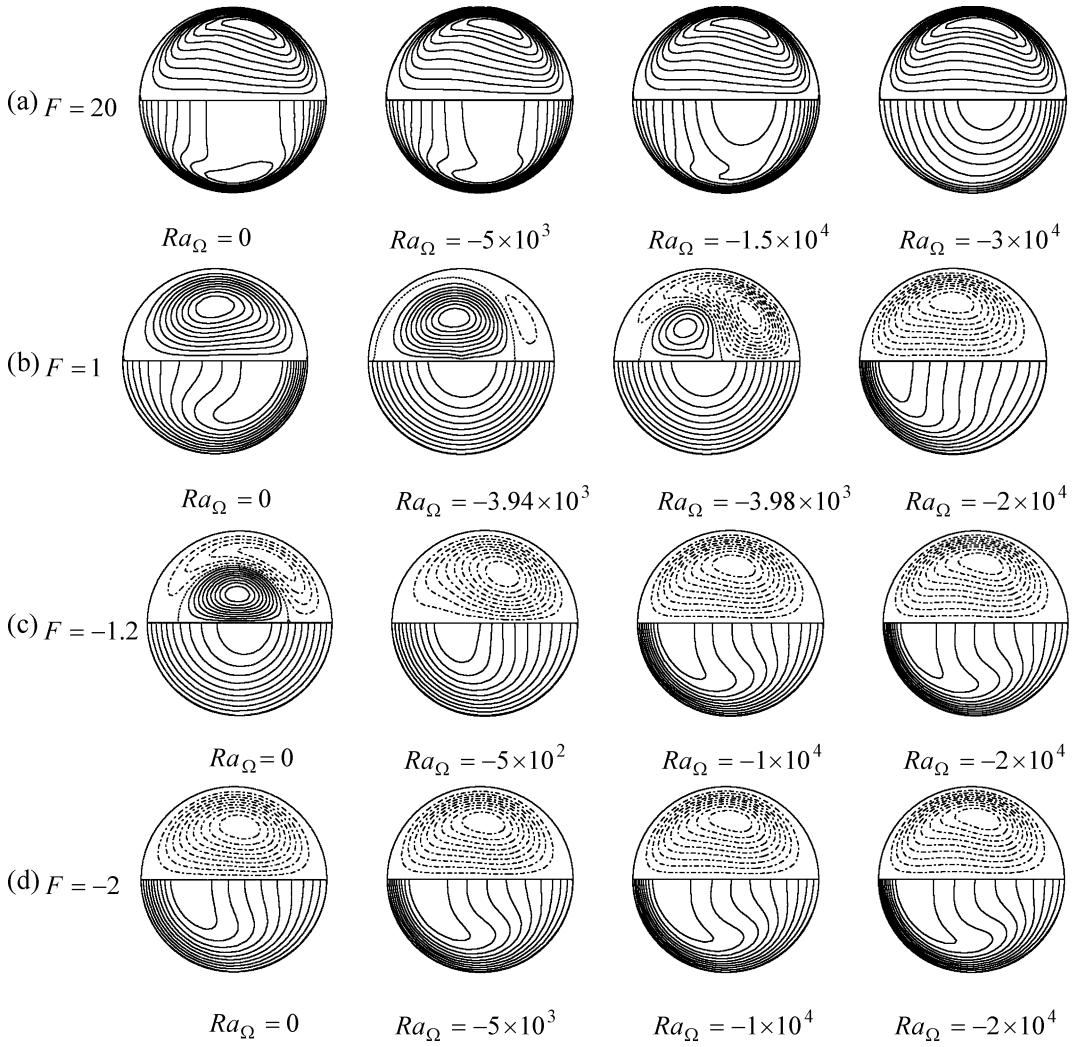

Fig. 8. Contours of secondary flow (upper-half) and axial velocity (lower half) for $Dn = 100$, $\kappa = 0.2$.

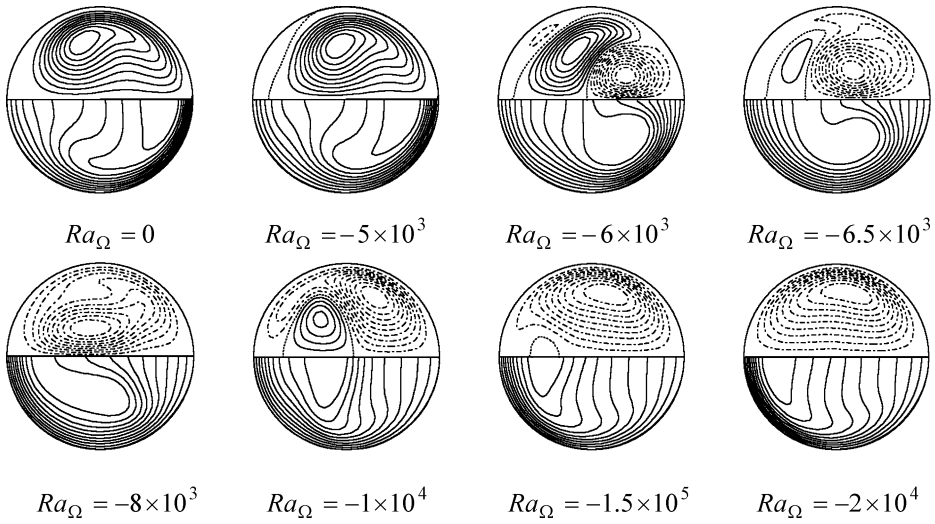

Fig. 9. Contours of secondary flow (upper-half) and axial velocity (lower half) for $Dn = 500$, $\kappa = 0.2$ and $F = -0.5$.

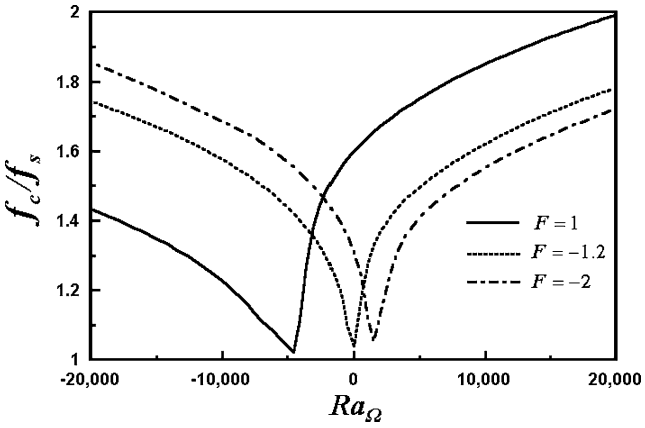

Fig. 10. Variation of friction factor ratio with Ra_Ω ($Dn = 100$, $\kappa = 0.2$).

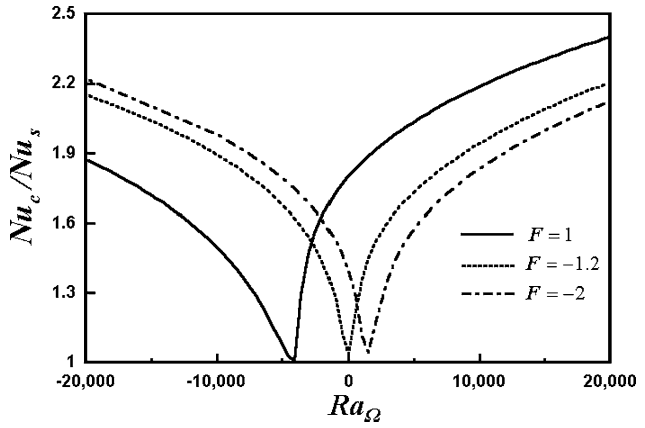

Fig. 11. Variation of Nusselt number ratio with Ra_Ω ($Dn = 100$, $\kappa = 0.2$).

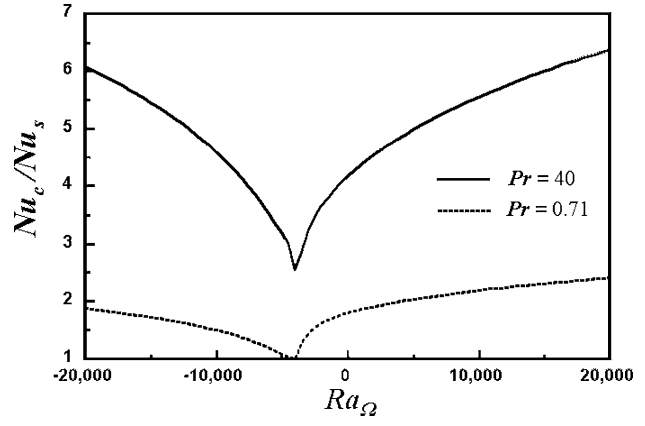

Fig. 12. Variation of Nusselt number ratio with Ra_Ω for different Pr ($Dn = 100$, $\kappa = 0.2$).

The case without the effect of buoyancy force: For co-rotation, the increasing F first exerts the same effect as the increasing Dean number and as F increases further, the Taylor–Proundman effects appear. But for the counter-rotating pipe, when $F \approx -1$, two kinds of secondary flow due to centrifugal force and Coriolis force can coexist and the axial velocity contours are just like that of Poiseulle flow. As F decreases further, the reversal flow behaviors emerge.

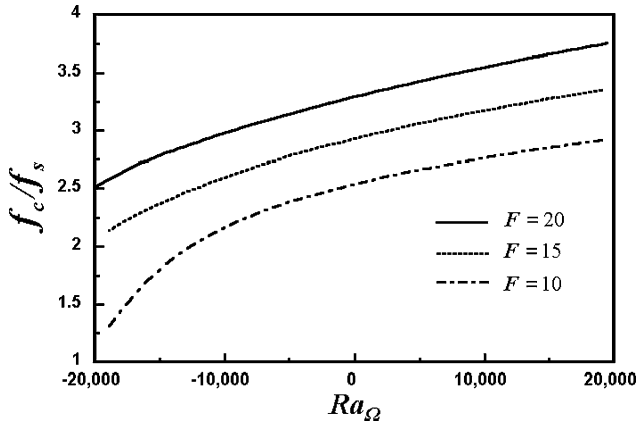

Fig. 13. Variation of friction factor ratio with Ra_Ω for a high rotating speed ($Dn = 100$, $\kappa = 0.2$).

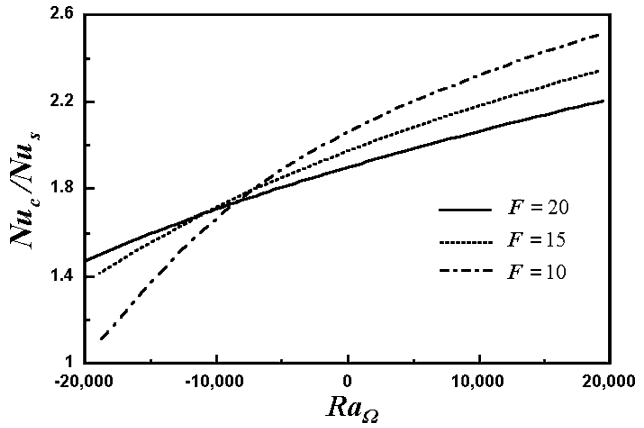

Fig. 14. Variation of Nusselt number ratio with Ra_Ω for a high rotating speed ($Dn = 100$, $\kappa = 0.2$, $Pr = 0.71$).

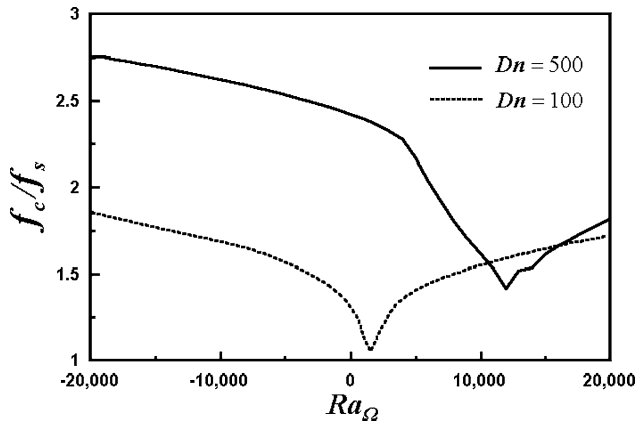

Fig. 15. Variation of friction factor ratio with Ra_Ω for different Dn ($F = -2$, $\kappa = 0.2$).

For a large Dean number, when $F \approx -1$, the Dean instability will appear.

If the fluid is heated, the secondary flow due to centrifugal force is intensified. For the co-rotation, the resultant secondary flow almost keeps the same structure. But for the counter-rotation, the coexistence of two secondary flows

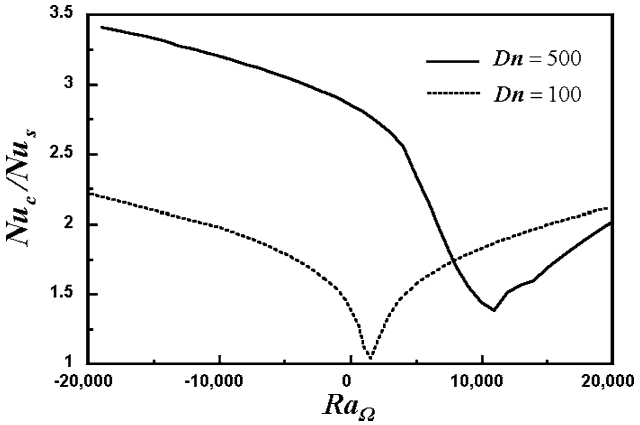

Fig. 16. Variation of Nusselt number ratio with Ra_{Ω} for different Dn ($F = -2$, $\kappa = 0.2$, $Pr = 0.71$).

could also appear at a certain value of Ra_{Ω}. The phenomena of Dean instability do not appear in this case for a large Dean number.

If the pipe is cooled, the buoyancy force has the opposite direction with centrifugal force. For the co-rotation, the opposite buoyancye-force driven secondary flow will weaken those due to Coriolis force and centrifugal force. But for the counter-rotation, it will intensify that due to Coriolis force. In this case, for a large Dean number, the opposite secondary flow due to inward buoyancy force could also be the disturbance, which makes the Dean instability to appear.

The response of the thermal structure to flow structure is depending on the Prandtl number, when Pr is small, the temperature profile is similar to the axial velocity profile and when Pr is large, axial velocity almost can be ignored and the secondary flow governs the heat transfer characteristics.

When the secondary flow reversal occurs, the friction factor and the Nusselt number almost reaches their minimum values and for a moderate Dean number, they almost have the same values with those in a non-rotating straight pipe. The effects of heating or cooling on the friction factor and the Nusselt number are dependent on F.

Acknowledgements

The authors wish to thank the financial support of the National Natural Science Foundation of P.R. China (Grant No: 10272096).

References

[1] W.R. Dean, Note on the motion of fluid in a curved pipe, Philos. Mag. 7 (4) (1927) 208–223.
[2] W.R. Dean, The stream-line motion of fluid in a curved pipe, Philos. Mag. 7 (5) (1928) 673–695.
[3] S.A. Berger, L. Talbot, L.S. Yao, Flow in a curved pipe, Ann. Rev. Fluid Mech. 15 (1983) 410–512.
[4] K. Nandakumar, J.H. Masiyah, Swirling flow and heat transfer in oiled and twisted pipe, in: A.S. Mujumdar, R.A. Mashelkar (Eds.), Advances in Transport Processes, Vol. 4, Wiley, New York, 1986, pp. 49–112.
[5] H. Ito, Flow in curved pipe, Japan Soc. Mech. Engng. Internat. J. 30 (1987) 543–552.
[6] S. A. Berger, Flow and heat transfer in curved pipes and tubes, AIAA Paper, 1991 91-0030.
[7] H. Ludwieg, Die Ausgebildete Kanalstromung in einem Rotierenden system, Ingenieur-Archiv 19 (1951) 296–308.
[8] L.M. Hocking, Boundary and shear layers in a curved rotating pipe, J. Math. Phys. Sci. 1 (1967) 123–136.
[9] H. Ito, T. Motai, Secondary flow in a rotating curved pipe, Rep. Inst. High Speed Mech. 29 (1974) 33–57.
[10] H. Ito, H. Aakita, S. Hasegawa, M. Suzuki, Numerical and experimental study on laminar flow in a rotating curved pipe (1. Constant Dean number), Mem. Inst. High Speed Mech. 58 (1987) 185–235.
[11] H. Ito, H. Aakita, S. Hasegawa, M. Suzuki, Numerical and experimental study on laminar flow in a rotating curved pipe (2. Constant rotational Reynolds number), Mem. Inst. High Speed Mech. 59 (1988) 45–96.
[12] P. Daskopoulos, A.M. Lenhoff, Flow in curved ducts, Part 2. Rotating ducts, J. Fluid Mech. 217 (1990) 575–593.
[13] M. Selmi, K. Nandakumar, W.H. Finlay, A bifurcation study viscous flow through a rotating curved duct, J. Fluid Mech. 262 (1994) 353–375.
[14] H. Ishigaki, Fundamental characteristics of laminar flows in a rotating curved pipe, Trans. JSME 59-561-B (1993) 1494–1501.
[15] H. Ishigaki, Laminar flow in rotating curved pipes, J. Fluid Mech. 329 (1996) 373–388.
[16] H. Ishigaki, Laminar convective heat transfer in rotating curved pipes, JSME Internat. J. Ser. B 42 (1999) 489–497.
[17] J.S. Zhang, X.R. Shen, B.Z. Zhang, The flow in rotating curved pipe, J. Hydrodynam. Ser. B 12 (1) (2000) 108–116.
[18] H. Miyazaki, Combined free and force convective heat transfer and fluid flow in rotating curved circular tube, Internat. J. Heat Mass Transfer 14 (1971) 1295–1309.
[19] H. Miyazaki, Combined free and forced convective heat transfer and fluid flow in a rotating curved rectangular tube, Trans. ASME C: J. Heat Transfer 95 (1973) 64–71.
[20] L.Q. Wang, K.C. Cheng, Flow transition and combined free and forced convective heat transfer in rotating curved channels: The case of positive rotation, Phys. Fluids 8 (1996) 1153–1173.
[21] Patankar, Numerical Heat Ransfer and Fluid Flow, Hemisphere, New York, 1980.
[22] J.S. Zhang, Studies on the characteristics of the viscous flow in rotating curved pipes, Ph.D. Thesis, Zhejiang University, 2001.